Elucidating the boundary layer turbulence dissipation rate using high-resolution measurements from a radar wind profiler network over the Tibetan Plateau

Deli Meng[1,2], Jianping Guo[1,3*] Xiaoran Guo[1*], Yinjun Wang[1], Ning Li[1], Yuping Sun[1], Zhen Zhang[1], Na Tang[1], Haoran Li[1], Fan Zhang[1], Bing Tong[3], Hui Xu[1], Tianmeng Chen[1]

[1]State Key Laboratory of Severe Weather, Chinese Academy of Meteorological Sciences, Beijing 100081, China

[2]High Impact Weather Key Laboratory of CMA, Changsha 410073, China

[3] Fujian Key Laboratory of Severe Weather, Fujian Institute of Meteorological Sciences, Fuzhou 350028, China

[4]State Key Laboratory of Urban and Regional Ecology, Research Center for Eco-Environmental Sciences, Chinese Academy of Sciences, Beijing 100085, China

Correspondence to: Dr/ Prof. Jianping Guo (Email: jpguocams@gmail.com)

Dr. Xiaoran Guo (Email: guoxiaoran2018@hotmail.com)

Abstract

The planetary boundary layer (PBL) over the Tibetan Plateau (TP) exerts a significant influence on regional and global climate, while its vertical structures of turbulence and evolution features remain poorly understood, largely due to the scarcity of observation. This study examines the vertical profile and daytime variation of turbulence dissipation rate (ε) in the PBL and free troposphere over the TP using the high-resolution (6 min and 120 m) measurements from the radar wind profiler (RWP) network, combined with the hourly data from the ERA5 reanalysis during the period from September 1, 2022 to October 31, 2023. Observational analyses show that the magnitude of ε below 3 km under all-sky conditions exhibits a large spatial discrepancy over the six RWP stations over the TP. Particularly, the values of ε at Minfeng and Jiuquan over the northern TP and Dingri over the southern TP are roughly an order of magnitude greater than those at Lijiang, Ganzi and Hongyuan over the eastern TP. This could be partially attributed to the difference in land cover across the six RWP stations. In terms of the diurnal variation, ε rapidly intensifies from 0900 local standard time (LST) to 1400 LST, and then gradually levels off in the late afternoon. Under clear-sky conditions, both ε and planetary boundary layer height (z_i) are greater, compared with cloudy-sky conditions, which could be due to the cooling effect by cloud that reduces the solar irradiation reaching the surface. In the lower PBL ($0.3 \leqslant z/z_i \leqslant 0.5$), where z is the height above ground level, the dominant influential factor for the development of turbulence is the surface-air temperature difference ($T_s - T_a$). By comparison, in the upper PBL ($0.6 \leqslant z/z_i \leq 1.0$), both the $T_s - T_a$ and vertical wind shear (VWS) affect the development of turbulence. Above the PBL ($1.0 < z/z_i \leq 2.0$), the shear production resulting from VWS dominates the variation of turbulence. Under cloudy-sky conditions, the reduced $T_s - T_a$ and weakened surface sensible heat flux tend to inhibit the turbulent motion in the PBL. On the other hand, the strong VWS induced by clouds enhances the turbulence above the PBL. The findings obtained here underscore the importance of RWP network in revealing the fine-scale structures of the PBL over the TP and gaining new insight into the PBL evolution.

1. Introduction

Turbulence ranks among the most intricate phenomena within the atmosphere, ensuring that the planetary boundary layer (PBL) remains thoroughly mixed during daylight hours (Li et al., 2023). As a result, the structure of the PBL is, to a considerable extent, governed by the evolution of turbulence (Teixeira et al., 2021). Turbulence dissipation rate (ε) reflects the amount of turbulent kinetic energy (TKE) that is converted into heat at the Kolmogorov scale and is a measure of the turbulence intensity (McCaffrey et al., 2017; Muñoz-Esparza et al., 2018). Proper parameterizations of the turbulence dissipation term with the aid of observations have great impacts on the forecast skill of weather and climate models, as ε strongly affects vertical turbulent mixing through its influence on TKE (Yang et al., 2017). Accurate estimation of ε is crucial for understanding the structure of turbulence in the PBL. To date, a variety of instruments have been used to observe or retrieve the vertical profiles of ε, including sodar, radar wind profiler (RWP), radiosonde, Doppler wind lidar (DWL) and ultrasonic anemometer (Jacoby-Koaly et al., 2002; Dodson and Griswold, 2021; Lv et al., 2021; Kotthaus et al., 2023). Compared with the DWL, the RWP exhibits better capability in capturing the turbulence structures in the cloudy sky. Furthermore, it is hard for radiosondes and ultrasonic anemometers to get the temporal continuous measurements of atmospheric turbulence, due to the high costs.

The Tibetan Plateau (TP), with an averaged elevation greater than 4,000m above sea level (ASL) and an area of approximately 2.5 million km^2, is towering into the lower and middle troposphere (Huang et al., 2023). By receiving a greater amount of solar shortwave radiation, the surface layer of the TP can transfer more heat through the PBL to the free atmosphere (Wang et al., 2015; Ma et al., 2023). The PBL over the TP exhibits strong convective thermals of warm air and upward motions due to the lower air density and buoyancy effect, which results in significant turbulence motions and turbulence-convection interactions with "popcorn" cloud structures (Xu et al., 2002; Xu et al., 2023). Understanding the statistical behavior of ε is key to revealing the vertical structure and evolution of PBL turbulence, which could improve the parameterization of PBL processes over the TP (Wang et al., 2015; Xu et al., 2019; Zhao et al., 2019; Ma et al., 2023). However, due to the limited observations of turbulence profiles, the daytime variation characteristics of ε over the TP and its main influencing mechanisms remain poorly understood.

A vast range of previous studies have attempted to figure out the mechanisms behind the turbulence, but most of them are based on radiosonde measurements or model simulation or reanalysis data (e.g., Banerjee et al., 2018; Che and Zhao, 2021; Wang et al., 2023a). A myriad of driving mechanisms is proposed to account for the PBL development over the TP, such as surface thermal and dynamic forcing, atmosphere stability, among others (Chen et al., 2016; Lai et al., 2021; Wang and Zhang, 2022; Chechin et al., 2023; Wang et al., 2023a). It has been demonstrated that the buoyancy term contribution on the southern slope of the TP is significantly larger than that on the southeastern edge of the TP (Wang et al., 2015). A larger surface-air temperature difference ($T_s - T_a$) and sensible heat flux promotes the rapid growth of deep PBL in the western and southern TP (Chen et al., 2013, 2016; Wang et al., 2016; Li et al., 2017a; Zhang et al., 2022).

Except for the above-mentioned thermal and dynamic effects, cloud radiative effect is found to be another significant factor that can dramatically modulate the evolution of daytime PBL turbulence (Bodenschatz et., 2010; Davis et al., 2020). For instance, cloud radiative forcing accounts for the rapid morning transition from stable to unstable PBL, thereby notably affecting the diurnal variation of the PBL (Su et al., 2023). Notably, longwave radiative cooling at the top of stratocumulus clouds can enhance turbulent diffusion within the stratocumulus topped PBL (Sun et al., 2016). A recent observational study suggests that cloud radiative cooling contributed about 32% to turbulent mixing even near the surface (Huang et al., 2020). In other words, cloud radiative processes, including entrainment and radiative cooling, can affect the TKE in the atmosphere (Nicholls et al., 1986; Sedlar et al., 2022; Chechin et al., 2023).

The TP is characterized by a high frequency of cumulus clouds which is about five times the regional mean over the other areas of China (Wang et al., 2015), and the occurrence frequency of clouds over the TP shows large diurnal and spatial variability, with the maxima in the afternoon in the eastern TP (Wan et al., 2022). The clouds have been found to significantly suppress the development of summer PBL in the early afternoon across China using fine-resolution radiosonde observations (Guo et al., 2019). Under continuous cloudy-sky conditions, the convective PBL develops slowly due to the smaller surface sensible heat compared to clear-sky conditions (Wang and Zhang, 2022). The turbulence motion in the PBL and its dynamic structure contribute to the formation and development of the popcorn-like convective clouds (Xu et al., 2002; Wang et al., 2020). Compared with eastern China, the more occurrence of low cloud in the afternoon over the TP is found to facilitate the PBL development, mainly owing to the lower atmospheric density (Wang et al., 2020).

However, the differences of turbulence vertical structures between clear-sky and cloudy-sky conditions are rarely explored, and the possible mechanism influencing the cloud topped PBL turbulence evolution remains unclear. To the best of our knowledge, most of the above-mentioned studies over the TP lack high-temporal resolution turbulence profile observations. Coincidently, the RWP network in China provides us a valuable opportunity to characterize the PBL turbulence structure over the TP (Guo et al., 2021a). Therefore, the main objective of this study is to resolve the above issues over the TP, by using observations from the RWP network together with other ground-based meteorological measurements and the ERA5 data. We also analyze the joint effect of thermodynamic and dynamic on ε structure in the daytime (0900–1700 local standard time, LST) PBL through $T_s - T_a$ and VWS.

The remainder of this manuscript proceeds as follows, Section 2 describes the data and methods used in this study. In Section 3, we analyze the spatio-temporal characteristics and daytime pattern of ε over the TP and investigate the possible thermodynamic and dynamic effect on PBL turbulence under clear-sky and cloudy-sky conditions. The summary and conclusions are given in section 4.

2. Data and methods

2.1 The RWP network over the TP

In this study, we use the vertical measurements of RWP data with a vertical resolution of 120 m and a temporal resolution of 6 min from the RWP network over the TP, which contains six operational stations (Minfeng, Jiuquan, Hongyuan, Ganzi, Lijang and Dingri) operated by the China Meteorological Administration (CMA) during the period from September 1, 2022 to October 31, 2023. The spatial distribution of the RWP network over the TP is shown in Fig. 1, and detailed information for each RWP station, including longitude, latitude, elevation, and land cover type is given in Table 1. Among these six RWP stations, the Dingri station is located in the foothills of the Himalayas with an elevation more than 4,300m ASL, dominated by the land cover of bare and alpine grassland. The Lijiang station is located in the southeastern TP characterized by complex terrain with an elevation of about 2,400m ASL. The Ganzi and Hongyuan stations are situated in the eastern TP, with elevations ranging from 3,300 to 3,500m ASL, and whose underlay is mainly alpine grassland. The Minfen and Jiuquan stations are situated in arid and semi-arid zones to the north of the TP, with elevations ranging from 1,400 to 1,500m, and their dominant underlying land cover is mainly bare land. Therefore, these two stations are well representative of the northern TP.

The RWP has the capability to obtain the high-temporal resolution atmospheric turbulence and wind profiles over the TP compared to the radiosonde and reanalysis, which makes it possible to analyze the fine PBL structures. The low and medium detection modes of RWPs can acquire the wind field and turbulence information bellow 5.0 km above ground level (AGL) (McCaffrey et al., 2017; Ruan et al., 2014). The RWP provides the radial observations (marked as RAD subset), including profiles of radial velocity, doppler spectral width, and signal-to-noise ratio (SNR). Also provided by the RWP is the real-time sampling data (marked as ROBS subset), including the profiles of horizontal wind (direction and speed), vertical velocity, and refractive index structure constant (Liu et al., 2020). There exist large uncertainties in the profiling measurements from RWP, thus the quality control for both RAD and ROBS subsets are indispensable before retrieving related dynamic variables over the TP (Liu et al., 2020; Wang et al., 2023). For instance, the profiling measurements highly deviate from the truth below 0.5 km AGL and above 5.0 km AGL, which are attributed to the near-surface clutter and significant beam attenuation, respectively (Guo et al., 2023). Thus, here only the RWP measurements at heights from 0.5 to 5.0 km are utilized for analysis.

2.2 Miscellaneous meteorological data

In this study, the hourly ground-based meteorological variables, including 2m air temperature (T_a), ground surface temperature (T_s), pressure and cloud cover, are derived from the six automatic weather stations over the TP. Also, 1 min rainfall observations from rain gauges are used to minimize the potential influence of rainfall on the profiling measurements from RWP. All these meteorological datasets are subjected to strict data-quality control by the National Meteorological Information Center (NMIC) of the CMA (Wang et al., 2023b). In addition, the hourly temperature data at pressure levels from the ERA5 reanalysis data is also used in this study (Hersbach et al., 2020).

2.3 Methods

2.3.1 Retrieval of turbulence dissipation rate

As a widely used ground-based equipment for detecting atmospheric wind profile (Liu et al., 2020), RWP has the advantage to estimate ε since it could measure Doppler velocity spectrum in the radar volume where the turbulence parcel motion accounts for the spectral width broadening (Jacoby-Koaly et al., 2002; White, 1999). In this study, the spectral width method is applied to retrieve ε from the RAD subset based on the underlying assumption that turbulence is isotropic, and the contributions to the spectral width from turbulent and non-turbulent process are independent of each other (Solanki et al., 2022; White, 1999).

The major steps for ε retrieval can be summarized as follows: (1) the spectral width variance consisting of the turbulence and non-turbulence variance is obtained from the spectral width measurements. (2) The non-turbulence broadening variances are decomposed into beam broadening variance due to the finite width of the beam, shear broadening variance generated by the presence of a wind gradient, and broadening variance arising from data processing, among others (Nastrom, 1997). (3) The turbulent broadening variance (σ_t^2) is extracted from the spectral width variance by excluding the above-mentioned non-turbulence broadening variances. (4) ε is estimated from σ_t^2 (White et al., 1999). For more details about the spectral width method, refer to the references (Jacoby-Koaly et al., 2002; McCaffrey et al., 2017; Nastrom, 1997; Solanki et al., 2021).

One caveat of the above-mentioned methods used to estimate ε lies in its sensitivity to the uncertainty in measuring horizontal wind speed, and the occurrence of negative value of σ_t^2, resulting in negative ε (i.e., invalid retrieval and should be discarded), which is previously documented (e.g., Chen et al., 2021; McCaffrey et al., 2017). It's noteworthy that ε estimates derived from the RWP lacks validation against in situ ε measurements from sonic anemometer in the aircraft or tower. This is another factor causing uncertainties that needs to be addressed in the future.

2.3.2 Estimation of planetary boundary layer height

The PBL height (hereafter referred to as z_i) is an important parameter for characterizing fine vertical structure of the PBL, which has important implications for the air mass exchange between the Earth's surface and the atmosphere aloft, thus affecting cloud development and air pollutant dispersion (Dai et al., 2014; Dodson and Griswold, 2021; Guo et al., 2021a; Li et al., 2017b; Wang et al., 2022).

Here daytime z_i at each RWP station is retrieved from the original SNR profiles from the RAD subset based on the improved threshold method (ITM), which is originally proposed by Liu et al. (2019). The steps are briefly outlined as follows. First of all, the original SNR profiles are normalized, leading to the profile of normalized SNR (NSNR), which is expected to avoid instrumental inconsistencies. Secondly, the NSNR threshold is set to 0.75 based on the z_i estimated by the radiosonde measurements at the same station. Thirdly, the profile of NSNR is scanned downward from the top to the ground surface. Finally, z_i is determined as the height where the NSNR profile is greater than 0.75 for the first time. For more details for the ITM, refer to Liu et al. (2019).

It is not optimal to retrieve z_i directly from the RWP measurements during nighttime, when the turbulence is weaker and SNR is stronger, leading to an overestimation of z_i (Duncan et al., 2022). The accuracy of the SNR data from RWP directly affects the accuracy of z_i. The z_i estimation for the ITM is particularly applicable in the daytime PBL (Bianco et al., 2008; Collaud Coen et al., 2014). The presence of clouds is proved to bring about uncertainty in z_i retrievals from the ITM, due to the challenge in identifying the peak from the NSNR profile (Angel et al., 2024). Notably, a convective cloud is accompanied by strong turbulence, which results in its boundary being misjudged as z_i.

2.3.3 Vertical wind shear

The ROBS subset is used to calculate VWS, which is an important parameter that presents the dynamical effect on the development of PBL (Zhang et al., 2020). VWS is given by

$$\mathrm{VWS} = \left[\left(\frac{\partial u}{\partial z}\right)^2 + \left(\frac{\partial v}{\partial z}\right)^2\right]^{1/2} \quad (1)$$

where u and v denote zonal and meridional wind component, respectively, z denotes the sample height AGL.

2.3.4 Classification of cloudy- and clear-sky conditions

Using RWP combined with the ground-based cloud cover observations at each station, the effect of clouds on daytime variations of PBL turbulence and z_i over the TP are investigated. Firstly, the 1 min precipitation and 6 min RWP data are time-matched to remove the profile data half an hour before and after the precipitation to obtain non-precipitation data (Wu et al, 2023). Then, all-sky conditions are defined as non-precipitation hours. Finally, the clear-sky (cloudy-sky) conditions are identified as hours with the cloud fraction less (greater) than 30% (80%), respectively (Guo et al., 2016; Solanki et al., 2021).

2.3.5 Calculation of the gradient Richardson number

The evolution of turbulence in the PBL has been previously recognized to be closely associated with atmospheric stability (Chechin et al., 2023; Chen et al, 2013; Lai et al., 2021; Muhsin et al., 2016). Therefore, we take the gradient Richardson number (Ri) as a variable to characterize atmospheric stability and the formation of turbulence over the TP. Following Stull (1988), Ri is formulated as follows:

$$Ri = \frac{g}{\theta_v}\frac{\partial\theta_v/\partial z}{(\partial u/\partial z)^2 + (\partial v/\partial z)^2} \quad (2)$$

where θ_v is the virtual potential temperature from ERA5, u and v are the hourly zonal and meridional wind components derived from RWP, respectively, g is the gravitational acceleration, and z represents the sample height AGL.

3. Results and discussion

3.1 Spatio-temporal distributions of daytime PBL turbulence dissipation rate

Both the PBL turbulence dissipation rate and z_i have significant diurnal variations over mountain and urban areas (Adler et al., 2014; Liu et al., 2019; Solanki et al., 2021; Yang et al., 2023). Since the longitude of the six stations over the TP ranges from 82.7°E to 102.6°E, it is necessary to use the LST to accurately capture the daytime variations of the PBL and make a comparison between different stations.

Figure 2 presents a comprehensive overview of the ε profile at 6 min intervals and hourly averaged z_i in lower troposphere at heights from 0.5 to 3.0 km for six RWP stations over the TP during the period from September 1, 2022 to October 31, 2023. As shown in the right panels of Fig. 2, ε generally decrease with increased height at all six RWP stations. The magnitude of ε and its vertical structures during the daytime at both Minfeng and Jiuquan stations over the northern TP and at Dingri station over the southern TP stand in stark contrast to those RWP stations (i.e., Lijiang, Ganzi and Hongyuan) in the eastern TP. It is apparent that ε exhibits a large spatial discrepancy. In terms of the latitudinal variation, the one-year averaged ε at the RWP stations in the east part of TP is smaller than in the western part of TP. In terms of the meridional variation, ε at the two RWP stations in the northern TP have a significantly larger magnitude than the other four stations. In particularly, the maximum mean value of daytime ε is found at Minfeng and Jiuquan in the northern TP, which reaches values up to $10^{-3.59}$ m^2 s^{-3} and $10^{-3.73}$ m^2 s^{-3}, respectively. By comparison, the lowest value of ε is found in the eastern TP, with the mean values of $10^{-4.06}$ m^2 s^{-3}, $10^{-4.30}$ m^2 s^{-3} and $10^{-4.22}$ m^2 s^{-3} at Lijiang, Hongyuan and Ganzi, respectively. Meanwhile, the mean magnitude of ε at Dingri in the southern TP lies between the magnitude of ε in the northern and eastern TP, which is $10^{-3.88}$ m^2 s^{-3}.

Overall, the spatial distribution of the z_i at all six RWP stations is clearly dependent on geographical location (Fig. 2), which resembles that of the ε. The geographic pattern of z_i from RWP agrees well with those from radiosonde measurements (Che and Zhao, 2021) and reanalysis (Slättberg, 2022). Of the six RWP stations, Dingri is located in the northern foothills of the Himalayas with an altitude of over 4300 m, where the bare land type results in a large surface sensible heat flux. This, together with the lowest atmospheric density, leads to the highest daytime mean value of z_i up to 2.10 km (Wang et al., 2015). The land surfaces at the Minfeng and Jiuquan stations in the northern TP are dominated by barren and relatively homogenous terrain, in sharp contrast to the highly vegetated terrain at the Ganzi and Hongyuan stations in the eastern TP (Fig. 1). The sparse vegetation in the northern TP generally comes with large Bowen ratio during the daytime, which tends to produce larger sensible heat flux compared to that in the eastern TP. The increased turbulence intensity in the PBL is generally associated with larger sensible heat flux, which has been reported by previous studies (Wang et al., 2016; Zhang et al., 2022). Therefore, the spatial and temporal variation of daytime ε over the TP are affected by the underlying surface type and air density.

Regarding the daytime pattern of turbulence (all six panels with color shading in Fig. 2), the turbulence over the TP shows a pronounced signature of single–peak variability. During the period 0900–1100 LST, the magnitude of ε at all six RWP stations is relatively weak. From 1100 LST onward, with the increase of downward solar shortwave radiation, surface sensible heat flux gradually rises, which leads to acceleration of turbulence mixing processes. Then, ε reaches peak in the early afternoon (1300–1500 LST). Afterwards, during the later afternoon (1500–1700 LST), ε diminishes gradually. Likewise, z_i almost follows the same daytime variation pattern of ε.

On the seasonal scale, the turbulence at the six RWP stations is characterized by significant variability, which is shown in Fig. S1. To be more specific, ε reaches the maximum in summer with the highest z_i, while touches the minimum in winter at Minfeng and Jiuquan. At the remaining four stations, the strongest ε is found in spring, as opposed to the weakest ε in autumn.

The above-mentioned findings imply that the turbulence intensity at the RWP stations over the northern and western TP is about one order of magnitude greater than that in the eastern TP. To further investigate the possible reasons for this significant difference in ε, the relationships between $T_s - T_a$ and ε for different regions are presented in Fig. 3. The mean value of $T_s - T_a$ in the northern and southern TP is 14.29°C, which is greater than that of eastern TP with the value of 11.26°C (Fig. 3a). The mean daytime ε for the two regions reaches up to $10^{-3.74}$ m^2 s^{-3} and $10^{-4.20}$ m^2 s^{-3}, respectively (Fig. 3b). Additionally, ε is significantly and positively correlated with $T_s - T_a$ (R>0.35, p<0.005), which illustrates that the thermal forcing makes an important contribution to turbulence development in the TP (Fig. 3c-d). As shown in Fig. S2, there is a positive correlation between the $T_s - T_a$ and ε, indicating that the thermal effect of the $T_s - T_a$ can promote the development of turbulence in at heights from 0.5 to 3.0 km under all-sky conditions. However, the relationship varies significantly between each RWP station. The slope values of the regression coefficients for the other five RWP stations, except for Hongyuan are all greater than 0.015. The maximum slope values are observed at Lijiang (0.029) and Dingri (0.027) in the southern TP, as compared with the minimum slope of 0.007 at Hongyuan. This suggests that near-surface thermal properties have nothing to do with ε at Hongyuan in the eastern TP.

Besides, the potential impact of VWS on ε is also examined, which is shown Fig. S3. Overall, VWS is found to positively correlate with ε at heights from 0.5 to 3.0 km under all-sky conditions, differing by RWP stations. The maximum slope values are observed at Lijiang (79.34) and Hongyuan (68.56), as compared with the minimum slope of 1.15 at Minfeng. Therefore, it can be inferred that atmospheric dynamic effect induced by VWS dominates the variability of ε at regions with the same underlying terrain and land over as Hongyuan.

3.2 Characteristics of daytime PBL turbulence dissipation rate under clear- and cloudy-sky conditions

The influence of clouds on the PBL properties has been discussed and analyzed in previous studies (e.g., Guo et al., 2016; Huang et al., 2023; Ma et al., 2023; Schumann et al., 1991; Yu et al., 2004). To reveal the potential impact of clouds on the PBL ε over the TP, the comparison analyses between clear- and cloudy-sky conditions are presented in this section. Figure 4 shows the daytime cycle of mean ε profile and z_i averaged over the six RWP stations under all-, clear- and cloudy-sky conditions. Overall, both the profile of ε and z_i under all-sky conditions over the TP present distinct single–peak variations, and their peaks approximately occur at 1400 LST (Fig. 4a). The daytime averaged ε below 3.0

km AGL is $10^{-3.95}$ m^2 s^{-3}, and mean z_i is 1.47 km, respectively. There is a significant positive correlation between ε and z_i during the daytime ($R=0.63$, $p<0.01$).

Under clear-sky condition, the daytime mean ε is $10^{-3.88}$ m^2 s^{-3} (Fig. 4b). During the period 1300–1500 LST, ε ranges from $10^{-3.43}$ to $10^{-2.82}$ m^2 s^{-3} ($10^{-4.17}$ to $10^{-3.40}$ m^2 s^{-3}) at heights from 0.5 km (1.0 km) to 1.0 km (2.0 km) in lower (upper) PBL. Thus, the well-mixed turbulence maintains the development of PBL in the early afternoon. By comparison, under cloudy-sky condition (Fig. 4c), the daytime mean value of z_i can reach up to 1.4 km, which is 0.12 km lower than that of clear-sky conditions. This means that the clouds would suppress the development of the PBL turbulence in the early afternoon which has been observed by the radiosonde observations described in Guo et al. (2016).

It is well known that there exists diurnal variation in PBL. To better reveal the mechanism how a myriad of geophysical parameters affect turbulence, the height-revolved ε retrievals are further normalized by the average PBL height. As noted above, the valid minimum altitude of the RWP is 0.5 km at 120 m vertical resolution, and the maximum z_i is approximately 2.0 km (Figs. 2&4). z is normalized by z_i to provide a nondimensional vertical coordinate for ε. It follows that z/z_i is great than 0.25, and the range of z/z_i is set from 0.3 to 2.0 for the following analyses.

The probability density distribution (PDF) of ε in the PBL ($0.3 \leqslant z/z_i \leq 1.0$) and above the PBL ($1.0<z/z_i \leq 2.0$) under all-, clear- and cloudy-conditions are given in Fig. 5. Overall, the mean ε are $10^{-3.82}$, $10^{-3.79}$ and $10^{-3.85}$ m^2 s^{-3} at the height range of $0.3 \leqslant z/z_i \leq 2.0$ under all-, clear- and cloudy-sky conditions, respectively (Fig. 5a). Within the PBL (Fig. 5b), the mean ε under clear-sky conditions ($10^{-3.27}$ m^2 s^{-3}) is greater than that of under cloudy-sky conditions ($10^{-3.36}$ m^2 s^{-3}), and the standard deviation of ε under clear-sky conditions is slightly greater than that under cloudy-sky conditions. This illustrates that clouds can significantly inhibit the turbulence intensity in the PBL, with the value of $\Delta\varepsilon$ between clear- and cloudy-sky conditions is -$10^{-4.0}$ m^2 s^{-3}. However, above the PBL (Fig. 5c), ε presents normal distribution characteristics, and there is no significant difference between the mean ε under clear- and cloudy-sky conditions.

To examine the overall impact of clouds on the vertical structure of turbulence within and above the PBL, Figure 5d shows the normalized contoured frequency by altitude diagram (NCFAD) of the $\Delta\varepsilon$ for normalized (z/z_i) profiles of ε between cloudy-sky and clear-sky conditions. Within the PBL, $\Delta\varepsilon$ is negative, and $|\Delta\varepsilon|$ generally decrease with increased z/z_i, where $\Delta\varepsilon$ is -10$^{-4.3}$ m^2 s^{-3} at z/z_i=0.5, and -10$^{-5.0}$ m^2 s^{-3} at z/z_i=1.0, respectively. This suggests that clouds may weaken turbulence within the PBL (Fig. 4b-c), especially in the lower PBL (z=820m, z/z_i<0.5). Figure S4 further shows the distinct spatial variability of cloud effect on ε across the six RWP stations. Particularly, the turbulence is weakened by clouds within the PBL at Minfeng and Jiuquan in the northern TP, as opposed to the enhanced ε within the PBL at Ganzi and Lijiang. This suggests that the cloud impact on ε is much complicated than expected. One of the reasons could be concerned with the cloud life stage, which is not dealt with in this present study. On top of the life stage, the cloud impact on ε, in combination with $T_s - T_a$ *and VWS*, exhibits a distinct altitude dependence, differing by RWP stations (Fig. S5).

3.3. Potential factors Influencing daytime PBL turbulence dissipation rate

3.3.1 Surface-air temperature difference

The vertical structure of PBL ε and z_i over the TP show obvious spatial differences in the context of a complex subsurface. The diverse land cover types lead to differences in surface albedo and soil moisture, which in turn lead to distinctions in thermodynamic characteristics such as sensible heat flux (Ma et al., 2023). Buoyant production driven by solar heating from the surface is one of the dominant sources generating turbulence in the convective PBL. The surface sensible heat flux is an important thermodynamic factor that affects the buoyant convective processes (Stull, 1988). Meanwhile, previous studies (e.g., Wang et al., 2022; Yang et al., 2023) have suggested that $T_s - T_a$ can serve as a good proxy for the sensible heat flux. There are not sensible heat flux measurements at six RWP stations in this study, and thus we directly take $T_s - T_a$ as a proxy thermodynamic variable to analyze its potential connection to variation of PBL turbulence.

Figure 6 shows the magnitude of ε varies as a function of $T_s - T_a$ for all six stations, within (0.3⩽z/z_i⩽1.0) and above (1.0<z/z_i≤2.0) the PBL, under all, clear- and cloudy-sky conditions, respectively. $T_s - T_a$ are first classified into five bins, which are then statistically analyzed against the corresponding ε averaged for z/z_i values between 0.3 and 2.0 to obtain regression equations incorporating slopes. Further, Table 2 shows the scatter plots between $Log_{10}\varepsilon$ (Figure 6) and $T_s - T_a$ (and VWS, Figure 7) at different altitude ranges under all-, clear- and cloudy-sky conditions. $Log_{10}\varepsilon$ is found to be linearly correlated with $T_s - T_a$ (and VWS) ($p<0.05$). The surface sensible heat flux generally increases with increased $T_s - T_a$, thus the increased $T_s - T_a$ intensifies the turbulence in PBL (0.3⩽z/z_i⩽1.0), which is shown in Fig. 6b, e, h. Within the PBL, ε is also positively correlated with $T_s - T_a$ whose slope values are larger than those at 0.3⩽z/z_i≤2.0. As $T_s - T_a$ rises, the larger surface sensible heat flux would lead to enhanced buoyancy process and turbulent motion within the PBL. On the other hand, ε above the PBL is negatively correlated with $T_s - T_a$ (Figs. 6c, f, i).This suggests that $T_s - T_a$ dramatically affects the development of turbulence within the PBL, whereas it has little effect on the turbulence above the PBL.

Within the PBL, the magnitude of slope (slope=0.019) under clear-sky conditions is larger than that of under-cloudy conditions (slope = 0.015) as shown in Figs. 6e and 6h. This implies that $T_s - T_a$ is the governing parameter rather than cloud cover affecting the PBL turbulence, particularly under the clear-sky conditions. Given that turbulence in the mixed PBL over the TP is usually driven by convection (Xu et al., 2023), as $T_s - T_a$ decreases when clouds are present, less heat is transferred from the surface to the atmosphere, reducing the buoyancy flux and leading to weaker turbulence in the PBL, especially for the lower PBL (0.3⩽z/z_i≤0.5), as shown in Figures 4b and 4c. Consequently, the clouds tend to suppress the development of PBL (Fig. 5a) and reduce z_i.

3.2.2 Vertical wind shear

Besides $T_s - T_a$, VWS is another crucial dynamic parameter that is related to the mechanical turbulence within the PBL. Similar to Fig. 6, Figure 7 presents the relationship between ε and VWS (both normalized by z_i) within and above the PBL under all-, clear-and cloudy-sky conditions, respectively. The near-surface clutter significantly increases the uncertainty of RWP data, which leads to incapability of analyzing the effect of wind shear on ε below 0.5 km AGL (z/z_i≥0.3) in the following sections.

Regardless of within or above the PBL, ε is positively correlated with VWS as shown in Fig. 7a, d, g and Tabel 2, which indicates that larger VWS leads to stronger turbulence. This suggests that the dynamic effect of VWS promotes the development of turbulence. Within the PBL (Figs. 7b, e, h), the slope of ε against VWS are smaller than at 0.3⩽ z/z_i≤2.0 with values ranging from 9.5 to 10.3. Above the PBL (Figs. 7c, f, i), the values of the slope are larger with values ranging from 10.7 to 18.1, which demonstrating that the dynamical effects of VWS influence the development of turbulence both within the upper PBL and above the PBL.

Under cloudy-sky conditions (Figs. 7h, i), the effect of VWS on turbulence within the upper PBL (Slope=10.3) is weaker than above the PBL (Slope=18.1), significantly. Compared to the clear-sky conditions (Figs. 7e, f), the values of the slopes are larger for that of under cloudy-sky conditions (Figs. 7h, i) both within and above the PBL. Remarkably, above the PBL, the effect of clouds on turbulence is more dramatic, as the slope value under cloudy-sky conditions is nearly twice as large as that of under clear-sky conditions. These results indicate the significant mechanical processes driven by VWS is important in the development of turbulence. A larger VWS in the PBL corresponds to stronger turbulence. Besides, above the PBL, the mechanical process of VWS is enhanced under cloudy-sky conditions.

3.2.3. Joint influence of $T_s - T_a$, VWS and atmosphere stability on ε

It was stated that turbulence can be produced by buoyant convective processes (i.e., thermals of warm air rising) and by mechanical processes (i.e., wind shear). From the previous section, it is known that $T_s - T_a$ and VWS both affect the development of PBL turbulence. Figure 8 gives the slope profiles of ε against $T_s - T_a$ and VWS at normalized heights (z/z_i) under all-, clear- and cloudy-sky conditions, respectively.

As inferred from the previous findings, $T_s - T_a$ primarily influences turbulence development within the PBL, irrespective of clear-sky and cloudy-sky conditions (Fig. 6). Figure 8a shows that the slope values within the PBL are predominantly positive, and the slope value decreases rapidly with height, which indicates that the influence of $T_s - T_a$ on PBL turbulence decreases with height. Interestingly, there is a nearly linear variation of the slope from the lower PBL to the top of the PBL. Within the PBL, the slope is positive, above the PBL, the slope becomes negative. This may be due to the linear decrease of heat flux transport and buoyancy term in the convective PBL (Stull, 1988). Therefore, these findings highlight the predominant thermal forcing of $T_s - T_a$ on turbulence development within the lower PBL. Fig 8 clearly shows the influence of cloud cover on the $T_s - T_a$ and the effect of the surface heating on the turbulence in the lower half of the PBL ($0.3 \leq z/z_i \leq 0.5$). While there is little difference for the clear-sky and cloudy-sky conditions when $z/z_i > 0.5$. Hence, under clear-sky conditions, the thermodynamic effect of $T_s - T_a$ is more pronounced within the lower PBL.

As shown in Fig. 7, it is evident that VWS influences turbulence development within and above the PBL. Figure 8b shows that when $0.3 \leq z/z_i \leq 2.0$, the slope values are consistently positive, indicating that VWS predominantly affects turbulence development within the mid-, upper- PBL and above the PBL. Moreover, when $0.3 \leq z/z_i \leq 1.2$, the slope values increase with height. However, when $1.4 < z/z_i \leq 2.0$, the slope decreases with height, which suggesting a diminishing influence of VWS. Additionally, within the PBL ($0.3 \leq z/z_i \leq 0.7$), the slope values under clear-sky conditions are close to those under cloudy-sky conditions, while the slope values under cloudy-sky conditions are even greater when $0.7 < z/z_i \leq 2.0$. For instance, when z/z_i=1.4, Slope$_{\text{Clear-sky}}$=14.6, while Slope$_{\text{Cloudy-sky}}$=27.0, indicating that the latter is 1.8 times larger than the former. These results suggest that clouds are primarily responsible for enhancing mechanical processes from VWS on turbulence within the upper PBL and above the PBL.

Furthermore, it can be concluded that, $T_s - T_a$ is the thermodynamic factor influencing turbulence development within the lower PBL ($0.3 \leq z/z_i \leq 0.5$), both $T_s - T_a$ and VWS jointly strengthen turbulence development in the upper PBL ($0.6 \leq z/z_i \leq 1.0$), and VWS emerges as the predominant factor affecting turbulence development above the PBL ($1.0<z/z_i\leq2.0$) (Figs. 8a, b).

The previous sections have revealed that hours of both high $T_s - T_a$ and strong wind shear would strengthen the turbulence within the PBL. Therefore, it's necessary to analyze the combined influence of thermodynamics and dynamics factors on the development of turbulence. Figure 9 presents the joint distribution of ε with $T_s - T_a$ and VWS within and above the PBL under all-, clear- and cloudy-sky conditions. Within the PBL (Figs. 9b, e, h), higher $T_s - T_a$ and VWS correspond to stronger turbulence (Fig. 8). In contrast, the thermodynamic effect of $T_s - T_a$ on turbulence has diminished and is no longer a dominant factor above the PBL, while the dynamical effect of VWS becomes the dominant factor (Figs. 9c, f, i). Compared to clear-sky conditions, both $T_s - T_a$ and VWS decrease under cloudy-sky conditions (Fig. 9h). This means that the weakening of both thermodynamic and dynamic effects leads to a decrease in turbulence, thereby inhibiting the development of turbulence within the PBL. Therefore, under cloudy-sky conditions, although the VWS is reduced, the dynamical effect of VWS on turbulence is strengthened (Figs. 7i and 8b), which in turn strengthens turbulence.

Since buoyant and mechanic forcing jointly influence the turbulence within the PBL, and VWS only represents the dynamic driving effect, it cannot accurately portray the effect of thermodynamic and dynamic effects on the PBL turbulence. The gradient Richardson number (Ri), on the other hand, is one of the important parameters characterizing atmospheric stability and can compare the buoyant turbulence production term and the shear production term in the form of a dimensionless ratio.

Similar to Fig. 9, the joint distribution of ε with $T_s - T_a$ and Ri within and above the PBL under all-sky, clear-sky and cloudy-sky conditions is given in Fig. 10. As shown in Fig. 10b, e, h, it is evident that the turbulence in the PBL tend to be enhanced for unstable conditions. Furthermore, under clear-sky conditions (Fig. 10e), the maximum number of samples is found when $Ri<1.0$ and $T_s - T_a>21.1$ in strongly unstable conditions, which may be caused by the buoyancy forcing driven by the larger $T_s - T_a$. By comparison, the effect of Ri on turbulence is relatively weakened above the PBL (Figs. 10c, f, i).

4 Summary and concluding remarks

This study investigates the characteristics of spatio-temporal distribution of daytime PBL turbulence dissipation rate (ε) based on more than one-year record (September 2022–October 2023) of profiling measurements from a radar wind profilers (RWP) network on the Tibet Plateau (TP). Also analyzed are the evolution of ε in the PBL and the possible influential mechanisms.

First of all, ε is firstly retrieved from the vertical wind measurements from RWP using the spectral width method. Afterwards, the spatial pattern of ε is examined. Results shows that the values of ε at the Minfeng and Jiuquan stations in the northern TP, and at Dingri over the southern TP are about one order of magnitude greater than those at the RWP stations of Lijiang, Ganzi and Hongyuan over the eastern TP. Coincidently, Minfeng and Junquan are dominated by bare or semiarid land, as opposed to the highly vegetation-covered land surface at Lijiang, Ganzi and Hongyuan. This suggests the spatial discrepancy of ε over the TP is highly relevant to the types of underlying land cover.

Although ε exhibits a variety of magnitudes among the six RWPs, the daytime pattern and vertical structure of ε are similar. Turbulence reaches the peak in the early afternoon (1300–1500 LST), coinciding with the highest PBL top. Under cloudy-sky conditions, the daytime mean value of ε is $10^{-4.02}$ m^2 s^{-3}, and the daytime mean value of the PBL height (z_i) can reach up to 1.40 km, which is 0.12 km lower than that of clear-sky conditions, indicating that clouds would suppress the development of the PBL turbulence.

As far as both the thermodynamic and dynamic forcings are concerned, surface-air temperature difference ($T_s - T_a$) and vertical wind shear (VWS) variables are examined by performing correlation analysis with ε. The slope values of ε against $T_s - T_a$ under clear-sky conditions is larger (slope=0.019) than under-cloudy conditions (slope = 0.013) within the PBL, while those values are negative above the PBL. The slope values of ε against VWS are positive regardless of within or above the PBL, where the largest value of 18.1 is observed above the PBL under cloudy-sky conditions, and the smallest value of 9.5 is observed in the PBL under clear-sky conditions.

Both the thermodynamic effect of $T_s - T_a$ and the dynamic effect of VWS enhance the development of turbulence under clear-sky or cloudy-sky conditions in the PBL. In the lower PBL (0.3⩽z/z_i≤0.5), $T_s - T_a$ has a larger positive slope with ε, which suggests that thermal forcing emerges as the dominant factor influencing development of the turbulence and PBL. By comparison, in the upper PBL (0.6⩽z/z_i≤1.0), $T_s - T_a$ and VWS jointly influence the development of turbulence, with larger $T_s - T_a$ leading to unstable atmospheric stability and stronger turbulence. Above the PBL (1.0<z/z_i≤2.0), VWS becomes the dominant factor influencing the development of turbulence. Compared to clear-sky conditions, on one hand, clouds would diminish $T_s - T_a$, resulting in decreased heat transfer from the surface to the PBL top, thereby weakening turbulence within the lower PBL (0.3⩽z/z_i≤0.5), inhibiting PBL development, and decreasing z_i. On the other hand, the stronger wind shear process would enhance the turbulence above PBL under the cloudy-sky conditions.

Although the above-mentioned findings of the PBL turbulence over the TP are the first results from profiling network observations to the best of our knowledge, fine-resolution spatial distribution remains unclear, largely due to the sparse distribution of RWP network on the TP. On top of this, the role of roughness length, vertical velocity, and entrainment remains unknown in the variation and evolution of atmospheric turbulence, which warrants further in-depth studies based on intensive field campaigns, in combination with theoretical analysis and numerical simulation experiments in the future.

Data Availability

The authors would like to acknowledge the National Meteorological Information Centre (NMIC) of China Meteorological Administration (CMA) (https://data.cma.cn) for providing the high-resolution radar wind profiler and ground-based meteorological data, which can be only accessed via registration. We are grateful to ECMWF for providing ERA5 hourly data (https://www.ecmwf.int/en/forecasts/datasets/reanalysis-datasets/era5/).

Acknowledgments

This work was jointly supported by the National Natural Science Foundation of China under grant 42325501, the High Impact Weather Key Laboratory of CMA, and NSFC under grants U2142209 and 42105090, the China Meteorological Administration Xiong'an Atmospheric Boundary Layer Key Laboratory under grant 2023LABL-B06, and Chinese Academy of Meteorological Sciences under grants 2021KJ008 and 2024Z003. Last but not least, we appreciated tremendously the constructive comments and suggestions made by the anonymous reviewers that significantly improved the quality of our manuscript.

Author Contributions

The study was completed with close cooperation between all authors. JG and XG conceived of the idea for this work. DM performed the analysis, DM and JG drafted the original manuscript with contributions from XG, NL, YS, ZZ and NT. YW, HL, FZ, BT, HX and TC provided useful suggestions and comments for the study and helped revise the manuscript.

Completing interests

The authors declare that they have no conflict of interest.

References

Adler, B. and Kalthoff, N.: Multi-scale transport processes observed in the boundary layer over a mountainous island, Bound.-Layer Meteor., 153, 515-537, https://doi.org/10.1007/s10546-014-9957-8, 2014.

Angel A C, Manoj M G. A novel method of estimating atmospheric boundary layer height using a 205 MHz VHF radar. Sci. Total. Environ., https://doi.org/10.1016/j.scitotenv.2023.168109, 907: 168109, 2024.

Banerjee, T., Brugger, P., De Roo, F., Kröniger, K., Yakir, D., Rotenberg, E., and Mauder, M.: Turbulent transport of energy across a forest and a semiarid shrubland, Atmos. Chem. Phys., 18, 10025–10038, https://doi.org/10.5194/acp-18-10025-2018, 2018.

Bianco, L., Wilczak, J. M., and White, A. B.: Convective boundary layer depth estimation from wind profilers: Statistical comparison between an automated algorithm and expert estimations, J. Atmos. Ocean. Technol., 25, 1397-1413, https://doi.org/10.1175/2008jtecha981.1, 2008.

Bodenschatz, E., Malinowski, S. P., Shaw, R. A., and Stratmann, F.: Can we understand clouds without turbulence? Science, 327, 970-971, https://doi.org/10.1126/science.1185138, 2010.

Che, J. H. and Zhao, P.: Characteristics of the summer atmospheric boundary layer height over the Tibetan Plateau and influential factors, Atmos. Chem. Phys., 21, 5253-5268, https://doi.org/10.5194/acp-21-5253-2021, 2021.

Chechin, D. G., Lüpkes, C., Hartmann, J., Ehrlich, A., and Wendisch, M.: Turbulent structure of the Arctic boundary layer in early summer driven by stability, wind shear and cloud-top radiative cooling: ACLOUD airborne observations, Atmos. Chem. Phys., 23, 4685-4707, https://doi.org/10.5194/acp-23-4685-2023, 2023.

Chen, X. L., Añel, J. A., Su, Z. B., de la Torre, L., Kelder, H., van Peet, J., and Ma, Y. M.: The deep atmospheric boundary layer and its significance to the stratosphere and troposphere exchange over the Tibetan Plateau, PLoS One, 8, 9, https://doi.org/10.1371/journal.pone.0056909, 2013.

Chen, X. L., Skerlak, B., Rotach, M. W., Añel, J. A., Su, Z., Ma, Y. M., and Li, M. S.: Reasons for the extremely high-ranging planetary boundary layer over the western Tibetan Plateau in winter, J. Atmos. Sci., 73, 2021-2038, https://doi.org/10.1175/jas-d-15-0148.1, 2016.

Chen, Z., Tian, Y., Wang, Y., Bi, Y., Wu, X., Huo, J., Pan, L., Wang, Y., and Lü, D.: Turbulence parameters measured by the Beijing mesosphere–stratosphere–troposphere radar in the troposphere and lower stratosphere with three models: comparison and analyses, Atmos. Meas. Tech., 15, 4785–4800, https://doi.org/10.5194/amt-15-4785-2022, 2022.

Collaud Coen, M., Praz, C., Haefele, A., Ruffieux, D., Kaufmann, P., and Calpini, B.: Determination and climatology of the planetary boundary layer height above the Swiss plateau by in situ and remote sensing measurements as well as by the COSMO-

2 model, Atmos. Chem. Phys., 14, 13205–13221, https://doi.org/10.5194/acp-14-13205-2014, 2014.

Dai, C., Wang, Q., Kalogiros, J. A., Lenschow, D. H., Gao, Z., and Zhou, M.: Determining boundary-layer height from aircraft measurements, Bound.-Layer Meteor., 152, 277-302, https://doi.org/10.1007/s10546-014-9929-z, 2014.

Davis E V, Rajeev K, and Mishra M K: Effect of clouds on the diurnal evolution of the atmospheric boundary-layer height over a tropical coastal station. Bound.-Layer Meteor., 175: 135-152, https://doi.org/10.1007/s10546-019-00497-6, 2020.

Dodson, D. S. and Griswold, J. D. S.: Turbulent and boundary layer characteristics during VOCALS-REx, Atmos. Chem. Phys., 21, 1937-1961, https://doi.org/10.5194/acp-21-1937-2021, 2021.

Duncan Jr., J. B., Bianco, L., Adler, B., Bell, T., Djalalova, I. V., Riihimaki, L., Sedlar, J., Smith, E. N., Turner, D. D., Wagner, T. J., and Wilczak, J. M.: Evaluating convective planetary boundary layer height estimations resolved by both active and passive remote sensing instruments during the CHEESEHEAD19 field campaign, Atmos. Meas. Tech., 15, 2479–2502, https://doi.org/10.5194/amt-15-2479-2022, 2022.

Guo, J. P., Li, Y., Cohen, J. B., Li, J., Chen, D. D., Xu, H., Liu, L., Yin, J. F., Hu, K. X., and Zhai, P. M.: Shift in the temporal trend of boundary layer height in China using long-term (1979-2016) radiosonde data, Geophys. Res. Lett., 46, 6080-6089, https://doi.org/10.1029/2019gl082666, 2019.

Guo, J. P., Miao, Y. C., Zhang, Y., Liu, H., Li, Z. Q., Zhang, W. C., He, J., Lou, M. Y., Yan, Y., Bian, L. G., and Zhai, P.: The climatology of planetary boundary layer height in China derived from radiosonde and reanalysis data, Atmos. Chem. Phys., 16, 13309-13319, https://doi.org/10.5194/acp-16-13309-2016, 2016.

Guo, J. P., Liu, B. M., Gong, W., Shi, L. J., Zhang, Y., Ma, Y. Y., Zhang, J., Chen, T. M., Bai, K. X., Stoffelen, A., de Leeuw, G., and Xu, X. F.: First comparison of wind observations from ESA's satellite mission Aeolus and ground-based radar wind profiler network of China, Atmos. Chem. Phys., 21, 2945-2958, https://doi.org/10.5194/acp-21-2945-2021, 2021a.

Guo, J. P., Zhang, J., Yang, K., Liao, H., Zhang, S. D., Huang, K. M., Lv, Y. M., Shao, J., Yu, T., Tong, B., Li, J., Su, T. N., Yim, S. H. L., Stoffelen, A., Zhai, P. M., and Xu,

X. F.: Investigation of near-global daytime boundary layer height using high-resolution radiosondes: first results and comparison with ERA5, MERRA-2, JRA-55, and NCEP-2 reanalyses, Atmos. Chem. Phys., 21, 17079-17097, https://doi.org/10.5194/acp-21-17079-2021, 2021b.

Guo, X. R., Guo, J. P., Zhang, D. L., and Yun, Y. X.: Vertical divergence profiles as detected by two wind-profiler mesonets over East China: Implications for nowcasting convective storms, Q. J. R. Meteorol. Soc., 149, 1629-1649, https://doi.org/10.1002/qj.4474, 2023.

Hersbach, H., Bell, B., Berrisford, P., Hirahara, S., Horányi, A., Muñoz-Sabater, J., Nicolas, J., Peubey, C., Radu, R., Schepers, D., Simmons, A., Soci, C., Abdalla, S., Abellan, X., Balsamo, G., Bechtold, P., Biavati, G., Bidlot, J., Bonavita, M., De Chiara, G., Dahlgren, P., Dee, D., Diamantakis, M., Dragani, R., Flemming, J., Forbes, R., Fuentes, M., Geer, A., Haimberger, L., Healy, S., Hogan, R. J., Hólm, E., Janisková, M., Keeley, S., Laloyaux, P., Lopez, P., Lupu, C., Radnoti, G., de Rosnay, P., Rozum, I., Vamborg, F., Villaume, S., and Thépaut, J. N.: The ERA5 global reanalysis, Q. J. R. Meteorol. Soc., 146, 1999-2049, https://doi.org/10.1002/qj.3803, 2020.

Huang, J. P., Zhou, X. J., Wu, G. X., Xu, X. D., Zhao, Q. Y., Liu, Y. M., Duan, A. M., Xie, Y. K., Ma, Y. M., Zhao, P., Yang, S., Yang, K., Yang, H. J., Bian, J. C., Fu, Y. F., Ge, J. M., Liu, Y. Z., Wu, Q. G., Yu, H. P., Wang, B. B., Bao, Q., and Qie, K.: Global climate impacts of land-surface and atmospheric processes over the Tibetan Plateau, Rev. Geophys., 61, 39, https://doi.org/10.1029/2022rg000771, 2023.

Huang, T., Yim, S. H. L., Yang, Y., Lee, O. S. M., Lam, D. H. Y., Cheng, J. C. H., and Guo, J.: Observation of turbulent mixing characteristics in the typical daytime cloud-topped boundary layer over Hong Kong in 2019, Remote Sens., 12, 1533, https://doi.org/10.3390/RS12091533, 2020.

Jacoby-Koaly, S., Campistron, B., Bernard, S., Bénech, B., Girard-Ardhuin, F., Dessens, J., Dupont, E., and Carissimo, B.: Turbulent dissipation rate in the boundary layer via UHF wind profiler Doppler spectral width measurements, Bound.-Layer Meteor., 103, 361-389, https://doi.org/10.1023/a:1014985111855, 2002.

Kotthaus, S., Bravo-Aranda, J. A., Coen, M. C., Guerrero-Rascado, J. L., Costa, M. J., Cimini, D., O'Connor, E. J., Hervo, M., Alados-Arboledas, L., Jiménez-Portaz, M., Mona, L., Ruffieux, D., Illingworth, A., and Haeffelin, M.: Atmospheric boundary layer height from ground-based remote sensing: a review of capabilities and limitations, Atmos. Meas. Tech., 16, 433-479, https://doi.org/10.5194/amt-16-433-2023, 2023.

Lai, Y., Chen, X. L., Ma, Y. M., Chen, D. L., and Zhaxi, S. L.: Impacts of the westerlies on planetary boundary layer growth over a valley on the north side of the Central Himalayas, J. Geophys. Res.-Atmos., 126, 20, https://doi.org/10.1029/2020jd033928, 2021.

Li, Y., Y. Wu, J. Tang, P. Zhu, Z. Gao, and Y. Yang. Quantitative evaluation of wavelet analysis method for turbulent flux calculation of non-stationary series, Geophys. Res. Lett., 50(5), e2022GL101591, http://dx.doi.org/10.1029/2022GL101591, 2023.

Li, Z. G., Lyu, S. H., Wen, L. J., Zhao, L., Ao, Y. H., and Wang, S. Y.: Effect of a cold, dry air incursion on atmospheric boundary layer processes over a high-altitude lake in the Tibetan Plateau, Atmos. Res., 185, 32-43, https://doi.org/10.1016/j.atmosres.2016.10.024, 2017a.

Li, Z. Q., Guo, J. P., Ding, A. J., Liao, H., Liu, J. J., Sun, Y. L., Wang, T. J., Xue, H. W., Zhang, H. S., and Zhu, B.: Aerosol and boundary-layer interactions and impact on air quality, Natl. Sci. Rev., 4, 810-833, https://doi.org/10.1016/10.1093/nsr/nwx117, 2017b.

Liu, B. M., Guo, J. P., Gong, W., Shi, L. J., Zhang, Y., and Ma, Y. Y.: Characteristics and performance of wind profiles as observed by the radar wind profiler network of China, Atmos. Meas. Tech., 13, 4589-4600, https://doi.org/10.5194/amt-13-4589-2020, 2020.

Liu, B. M., Ma, Y. Y., Guo, J. P., Gong, W., Zhang, Y., Mao, F. Y., Li, J., Guo, X. R., and Shi, Y. F.: Boundary layer heights as derived from ground-based radar wind profiler in Beijing, IEEE Trans. Geosci. Remote Sensing, 57, 8095-8104, https://doi.org/10.1109/tgrs.2019.2918301, 2019.

Lv, Y. M., Guo, J. P., Li, J., Cao, L. J., Chen, T. M., Wang, D., Chen, D. D., Han, Y., Guo, X. R., Xu, H., Liu, L., Solanki, R., and Huang, G.: Spatiotemporal characteristics of atmospheric turbulence over China estimated using operational high-resolution soundings, Environ. Res. Lett., 16, 13, https://doi.org/10.1088/1748-9326/abf461, 2021.

Ma, Y. M., Yao, T. D., Zhong, L., Wang, B. B., Xu, X. D., Hu, Z. Y., Ma, W. Q., Sun, F. L., Han, C. B., Li, M. S., Chen, X. L., Wang, J. M., Li, Y. Q., Gu, L. L., Xie, Z. P., Liu, L., Sun, G. H., Wang, S. J., Zhou, D. G., Zuo, H. C., Xu, C., Liu, X., Wang, Y. J., and Wang, Z. Y.: Comprehensive study of energy and water exchange over the Tibetan Plateau: A review and perspective: From GAME/Tibet and CAMP/Tibet to TORP, TPEORP, and TPEITORP, Earth-Sci. Rev., 104312, 2023.

McCaffrey, K., Bianco, L., and Wilczak, J. M.: Improved observations of turbulence dissipation rates from wind profiling radars, Atmos. Meas. Tech., 10, 2595-2611, https://doi.org/10.5194/amt-10-2595-2017, 2017.

Muhsin, M., Sunilkumar, S. V., Ratnam, M. V., Parameswaran, K., Murthy, B. V. K., Ramkumar, G., and Rajeev, K.: Diurnal variation of atmospheric stability and turbulence during different seasons in the troposphere and lower stratosphere derived from simultaneous radiosonde observations at two tropical stations, in the Indian Peninsula, Atmos. Res., 180, 12-23, https://doi.org/10.1016/j.atmosres.2016.04.021, 2016.

Muñoz-Esparza, D., Sharman, R. D., and Lundquist, J. K.: Turbulence Dissipation Rate in the Atmospheric Boundary Layer: Observations and WRF Mesoscale Modeling during the XPIA Field Campaign, Mon. Weather Rev., 146, 351-371, https://doi.org/10.1175/mwr-d-17-0186.1, 2018.

Nastrom, G. D.: Doppler radar spectral width broadening due to beamwidth and wind shear, Ann. Geophys.-Atmos. Hydrospheres Space Sci., 15, 786-796, https://doi.org/10.1007/s00585-997-0786-7, 1997.

Nicholls, S.: The dynamics of stratocumulus: Aircraft observations and comparisons with a mixed layer model, Q. J. Roy. Meteor. Soc., 110, 783–820, https://doi.org/10.1002/qj.49711046603, 1984.

Ruan, Z., Mu, R. Q., Wei, M., and Ge, R. S.: Spectrum analysis of wind profiling radar measurements, J. Meteorol. Res., 28, 656-667, https://doi.org/10.1007/s13351-014-3171-y, 2014.

Sedlar, J., Riihimaki, L. D., Turner, D. D., Duncan, J., Adler, B., Bianco, L., Lantz, K., and Wilczak, J.: Investigating the impacts of daytime boundary layer clouds on surface energy fluxes and boundary layer structure during CHEESEHEAD19, J. Geophys. Res.-Atmos., 127, e2021JD036060, https://doi.org/10.1029/2021JD036060, 2022

Schumann, U. and Moeng, C. H.: Plume budgets in clear and cloudy convective boundary layers, J. Atmos. Sci., 48, 1758-1770, https://doi.org/10.1175/1520-0469(1991)048<1758:Pbicac>2.0.Co;2, 1991.

Slättberg, N., Lai, H. W., Chen, X. L., Ma, Y. M., and Chen, D. L.: Spatial and temporal patterns of planetary boundary layer height during 1979-2018 over the Tibetan Plateau using ERA5, Int. J. Climatol., 42, 3360-3377, https://doi.org/10.1002/joc.7420, 2022.

Solanki, R., Guo, J. P., Lv, Y. M., Zhang, J., Wu, J. Y., Tong, B., and Li, J.: Elucidating the atmospheric boundary layer turbulence by combining UHF radar wind profiler and radiosonde measurements over urban area of Beijing, Urban CLim., 43, 13, https://doi.org/10.1016/j.uclim.2022.101151, 2022.

Solanki, R., Guo, J. P., Li, J., Singh, N., Guo, X. R., Han, Y., Lv, Y. M., Zhang, J., and Liu, B. M.: Atmospheric-boundary-layer-height variation over mountainous and urban stations in Beijing as derived from radar wind-profiler measurements, Bound.-Layer Meteor., 181, 125-144, https://doi.org/10.1007/s10546-021-00639-9, 2021.

Stull, R. B.: Mean Boundary Layer Characteristics, in: An Introduction to boundary layer meteorology, edited by: Stull, R. B., Springer Netherlands, Dordrecht, 1–27, https://doi.org/10.1007/978-94-009-3027-8_1, 1988.

Su, T. N., Li, Z. Q., and Zheng, Y. T.: Cloud-Surface Coupling Alters the Morning Transition From Stable to Unstable Boundary Layer, Geophys. Res. Lett., 50, 9, https://doi.org/10.1029/2022gl102256, 2023.

Sun, W., Li, L., and Wang, B.: Reducing the biases in shortwave cloud radiative forcing in tropical and subtropical regions from the perspective of boundary layer processes, Sci. China Earth Sci., 59, 1427–1439, https://doi.org/10.1007/s11430-016-5290-z, 2016.

Teixeira, J., Piepmeier, J. R., Nehrir, A. R., Ao, C. O., Chen, S. S., Clayson, C. A., Fridlind, A. M., Lebsock, M., McCarty, W., Salmun, H., Santanello, J. A., Turner, D. D., Wang, Z., and Zeng, X.: Toward a global planetary boundary layer observing system: the NASA PBL incubation study team report, NASA PBL Incubation Study Team, 134 pp., available at: https://science.nasa.gov/science-red/s3fspublic/atoms/files/NASAPBLIncubationFinalReport.pdf, last access: 15 November 2021.

Wan, X., Zheng, J. F., Wan, R., Xu, G. R., Qin, J. F., and Yi, L.: Intercomparison of cloud vertical structures over four different stations of the eastern slope of the Tibetan Plateau in summer using Ka-band millimeter-wave radar measurements, Remote Sens., 14, 19, https://doi.org/10.3390/rs14153702, 2022.

Wang, C. X., Ma, Y. M., and Han, C. B.: Research on the atmospheric boundary layer structure and its development mechanism in the Tibetan Plateau, Adv. Atmos. Sci., 38, 414-428, 2023a.

Wang, M. Z. and Zhang, J. T.: The relationship among summer atmospheric boundary layer height over the Taklimakan Desert, its land surface parameters and Eurasian circulation, Atmos. Sci. Lett., 23, 13, https://doi.org/10.1002/asl.1122, 2022.

Wang, M. Z., Lu, H., Ming, H., and Zhang, J. T.: Vertical structure of summer clear-sky atmospheric boundary layer over the hinterland and southern margin of Taklamakan Desert, Meteorol. Appl., 23, 438-447, https://doi.org/10.1002/met.1568, 2016.

Wang, S. Q., Guo, J. P., Xian, T., Li, N., Meng, D. L., Li, H. J., and Cheng, W.: Investigation of low-level supergeostrophic wind and Ekman spiral as observed by a radar wind profiler in Beijing, Front. Environ. Sci., 11, 9, https://doi.org/10.3389/fenvs.2023.1195750, 2023b.

Wang, Y. J., Zeng, X. B., Xu, X. D., Xie, F. Q., and Zhao, Y.: Improving the estimate of summer daytime planetary boundary layer height over land from GPS radio occultation data, Geophys. Res. Lett., 49, 9, https://doi.org/10.1029/2021gl096304, 2022.

Wang, Y. J., Xu, X. D., Zhao, T. L., Sun, J. H., Yao, W. Q., and Zhou, M. Y.: Structures of convection and turbulent kinetic energy in boundary layer over the southeastern edge of the Tibetan Plateau, Sci. China-Earth Sci., 58, 1198-1209, https://doi.org/10.1007/s11430-015-5054-1, 2015.

Wang, Y. J., Zeng, X. B., Xu, X. D., Welty, J., Lenschow, D. H., Zhou, M. Y., and Zhao, Y.: Why are there more summer afternoon low clouds over the Tibetan Plateau compared to eastern China? Geophys. Res. Lett., 47, 10, https://doi.org/10.1029/2020gl089665, 2020.

White, A. B., Lataitis, R. J., and Lawrence, R. S.: Space and time filtering of remotely sensed velocity turbulence, J. Atmos. Ocean. Technol., 16, 1967-1972, https://doi.org/10.1175/1520-0426(1999)016<1967:Satfor>2.0.Co;2, 1999.

Wu, J. Y., Guo, J. P., Yun, Y. X., Yang, R. F., Guo, X. R., Meng, D. L., Sun, Y. P., Zhang, Z., Xu, H., and Chen, T. M.: Can ERA5 reanalysis data characterize the pre-storm environment? Atmos. Res., 297, 18, https://doi.org/10.1016/j.atmosres.2023.107108, 2024.

Xu, L. J., Liu, H. Z., Du, Q., and Xu, X. D.: The assessment of the planetary boundary layer schemes in WRF over the central Tibetan Plateau, Atmos. Res., 230, 12, https://doi.org/10.1016/j.atmosres.2019.104644, 2019.

Xu, X. D., Tang, Y., Wang, Y. J., Zhang, H. S., Liu, R. X., and Zhou, M. Y.: Triggering effects of large topography and boundary layer turbulence on convection over the Tibetan Plateau, Atmos. Chem. Phys., 23, 3299-3309, https://doi.org/10.5194/acp-23-3299-2023, 2023.

Xu, X. D., Zhou, M. Y., Chen, J. Y., Bian, L. G., Zhang, G. Z., Liu, H. Z., Li, S. M., Zhang, H. S., Zhao, Y. J., Suolong, D.J., and Wang, J. Z.: A comprehensive physical pattern of land-air dynamic and thermal structure on the Qinghai-Xizang Plateau, Sci. China Ser. D-Earth Sci., 45, 577-594, https://doi.org/10.1360/02yd9060, 2002.

Yang, B., Qian, Y., Berg, L. K., Ma, P. L., Wharton, S., Bulaevskaya, V., Yan, H. P., Hou, Z. S., and Shaw, W. J.: Sensitivity of Turbine-Height Wind Speeds to Parameters in Planetary Boundary-Layer and Surface-Layer Schemes in the Weather Research and Forecasting Model, Bound.-Layer Meteor., 162, 117-142, https://doi.org/10.1007/s10546-016-0185-2, 2017.

Yang, R. F., Guo, J. P., Deng, W. L., Li, N., Fan, J. H., Meng, D. L., Liu, Z., Sun, Y. P., Zhang, G. L., and Liu, L. H.: Investigation of turbulent dissipation rate profiles from two radar wind profilers at plateau and plain stations in the north China plain, Remote Sens., 15, 14, https://doi.org/10.3390/rs15164103, 2023.

Zhang, L., Zhang, H. S., Li, Q. H., Wei, W., Cai, X. H., Song, Y., Mamtimin, A., Wang, M. Z., Yang, F., Wang, Y., and Zhou, C. L.: Turbulent mechanisms for the deep convective boundary layer in the Taklimakan desert, Geophys. Res. Lett., 49, 9, https://doi.org/10.1029/2022gl099447, 2022.

Zhang, Y., Guo, J. P., Yang, Y. J., Wang, Y., and Yim, S. H. L.: Vertica wind shear modulates particulate matter pollutions: a perspective from radar wind profiler observations in Beijing, China, Remote Sens., 12, 17, https://doi.org/10.3390/rs12030546, 2020.

Zhao, P., Li, Y. Q., Guo, X. L., Xu, X. D., Liu, Y. M., Tang, S. H., Xiao, W. M., Shi, C. X., Ma, Y. M., Yu, X., Liu, H. Z., Jia, L., Chen, Y., Liu, Y. J., Li, J., Luo, D. B., Cao, Y. C., Zheng, X. D., Chen, J. M., Xiao, A., Yuan, F., Chen, D. H., Pang, Y., Hu, Z. Q., Zhang, S. J., Dong, L. X., Hu, J. Y., Han, S., and Zhou, X. J.: The Tibetan Plateau surface-atmosphere coupling system and its weather and climate effects: the third Tibetan Plateau atmospheric science experiment, J. Meteorol. Res., 33, 375-399, https://doi.org/10.1007/s13351-019-8602-3, 2019.

Table list

Table 1. Summary of the geographical conditions and land surface of the six radar wind profiler (RWP) stations over the Tibet Plateau (TP).

RWP station	Latitude (°E)	Longitude (°N)	Elevation (m)	Land cover types
Minfeng	82.69	37.07	1408.9	Bare land
Jiuquan	98.49	39.77	1477.2	Bare land
Dingri	87.07	28.39	4326.0	Grassland
Ganzi	100.00	31.62	3353.0	Bare land, grassland
Hongyuan	102.55	32.79	3465.0	Bare land, grassland
Lijiang	100.22	26.85	2382.4	Bare land, grass land

Table 2. Summary of the correlation of $\mathrm{Log}_{10}\varepsilon$ at different altitude ranges under all-, clear- and cloudy-sky conditions with $\mathrm{T_s} - \mathrm{T_a}$ and vertical wind shear (VWS) for all six RWP stations. The superscript * for R indicates that the regression slope is statistically significant at $\mathrm{p} < 0.01$.

Conditions	$Log_{10}\varepsilon$ VS $T_s - T_a$	$Log_{10}\varepsilon$ VS VWS
all-sky, 0.3≤z/z_i≤2.0	y=0.010x–4.05, R= 0.21*	y=13.6x–4.19, R=0.29*
all-sky, 0.3≤z/z_i≤1.0	y=0.018x–3.70, R=0.29*	y=13.2x–3.77, R=0.20*
all-sky, 1.0<z/z_i≤2.0	y=-0.004x–4.20, R=-0.09*	y=17.6x–4.57, R=0.36*
clear-sky, 0.3≤z/z_i≤2.0	y=0.011x–4.04, R=0.23*	y=10.7x–4.13, R=0.26*
clear -sky, 0.3≤z/z_i≤1.0	y=0.018x–3.67, R=0.30*	y=11.1x–3.70, R=0.17*
clear -sky, 1.0<z/z_i≤2.0	y=-0.005x–4.17, R=-0.11*	y=13.8x–4.52, R=0.34*
cloudy-sky, 0.3≤z/z_i≤2.0	y=0.009x–4.06, R=0.16*	y=18.5x–4.29, R=0.33*
cloudy-sky, 0.3≤z/z_i≤1.0	y=0.018x–3.71, R=0.26*	y=15.5x–3.84, R=0.23*
cloudy-sky, 1.0<z/z_i≤2.0	y=-0.004x–4.22, R=-0.08*	y=26.2x–4.67, R=0.42*

Figures

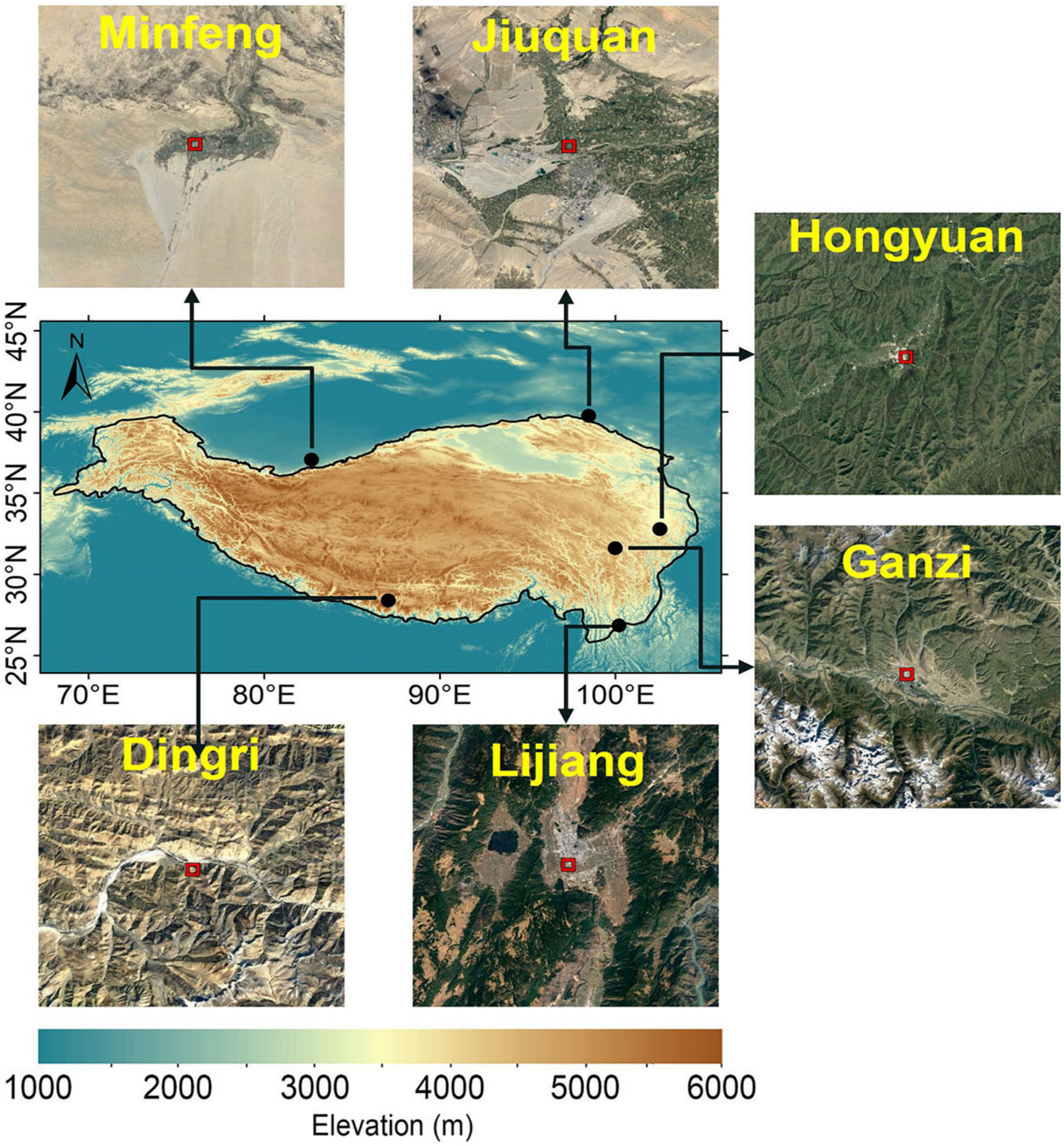

Figure 1. Spatial distribution of radar wind profiler (RWP) network comprised of six stations (in black solid circles) on the Tibetan Plateau (TP). The inset map surrounding the main frame denotes the RGB satellite image from Google Earth that is centered at each RWP station.

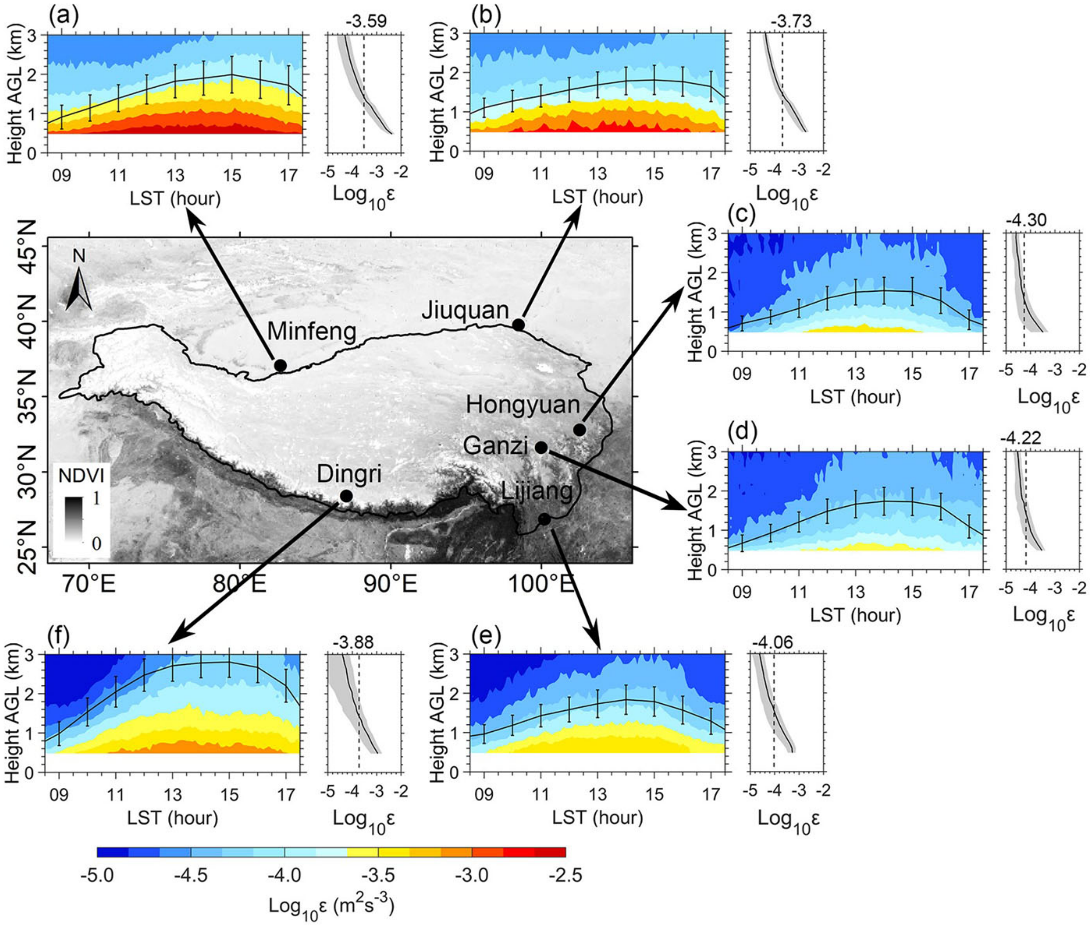

Figure 2. Spatial distribution of the diurnal evolution of the vertical profile of logarithmic turbulence dissipation rate ($Log_{10}\varepsilon$ in color shading, unit: m^2 s^{-3}) at 120 m vertical resolution and 6 min intervals, and hourly mean planetary boundary layer height (z_i, black line, unit: km) during daytime under all-sky conditions from 0900 to 1700 LST for the period September 2022 to October 2023 as retrieved from the profiling measurements at six RWP stations over the TP. The vertical bars indicate the 0.5 standard deviations for z_i. Also shown on the right-hand side panel are temporally averaged vertical profile of ε (black line) and its corresponding one standard deviation (gray shading).

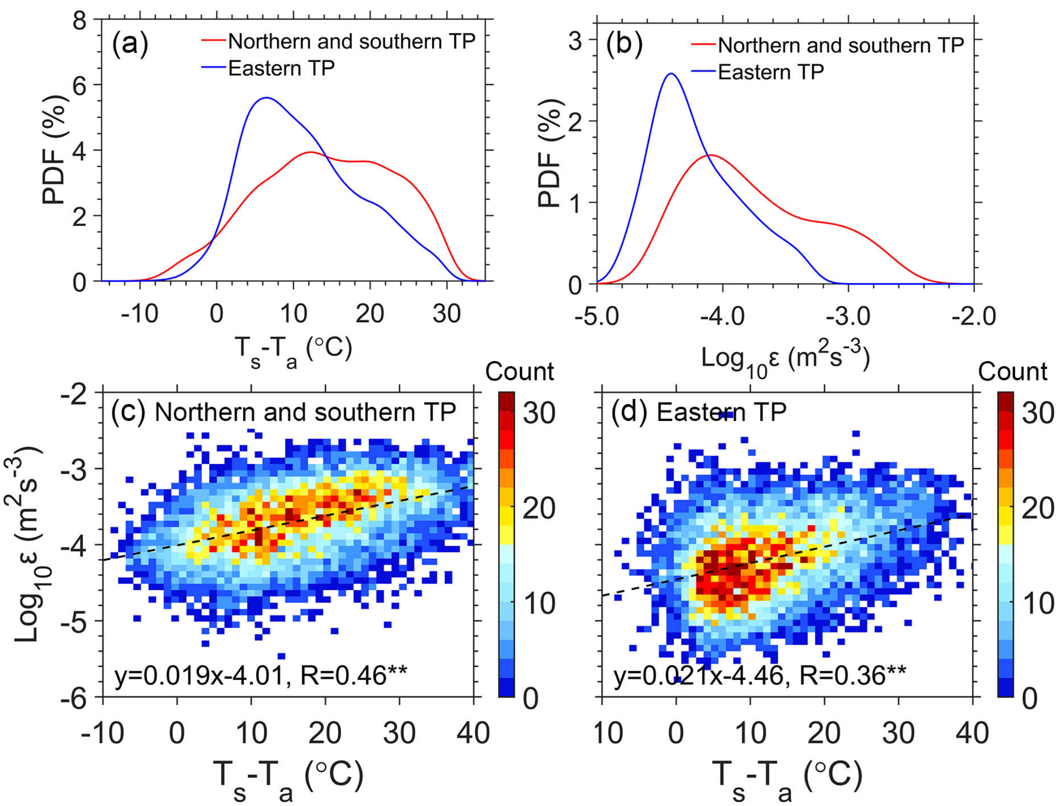

Figure 3. (a) PDF of surface-air temperature difference ($T_s - T_a$) for the northern and southern TP (red line) and eastern TP (blue line), (b) same as (a), but for PDF of $Log_{10}\varepsilon$ estimated from the measurements of radar wind profilers (RWPs) at the heights ranging from 0.5 to 3.0 km, (c) scatter plots of $Log_{10}\varepsilon$ as a function of $T_s - T_a$ in the northern and southern TP, (d) same as (c), but for the eastern TP during daytime under all-sky conditions from 0900 to 1700 local standard time (LST) for the period September 2022 to October 2023. The superscript ** for R indicates that the regression slope is statistically significant at $p < 0.01$ level.

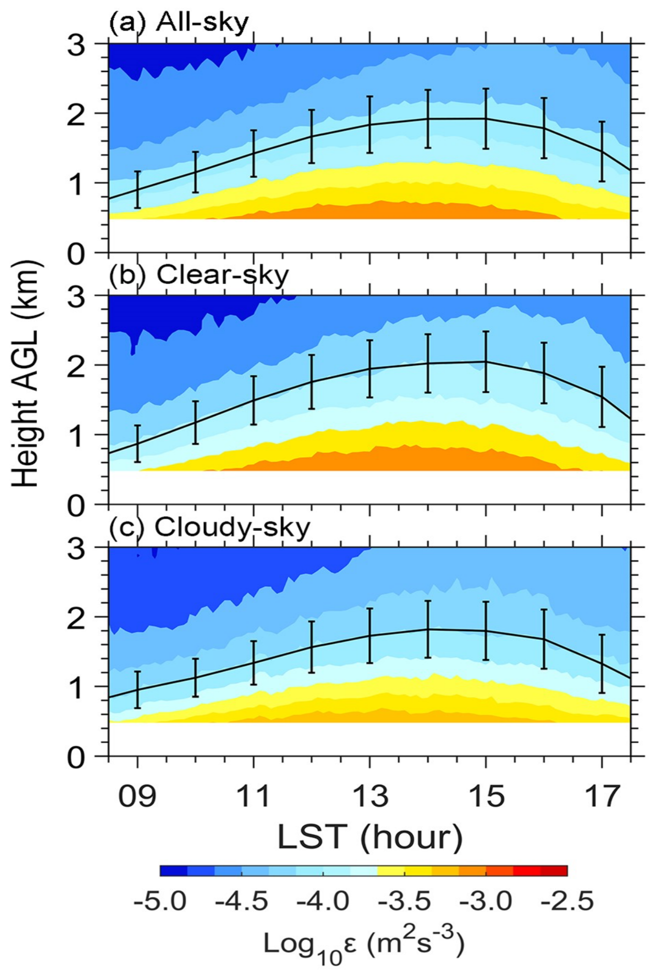

Figure 4. Diurnal evolution of the vertical profile of $Log_{10}\varepsilon$ (color shading, unit: m^2 s^{-3}) and z_i (solid line, unit: km) averaged over the six RWP stations over the TP during daytime from 0900 to 1700 LST for the period September 2022 to October 2023 for (a) all-sky conditions, (b) clear-sky conditions and (c) cloudy-sky conditions. The vertical bars indicate the 0.5 standard deviations.

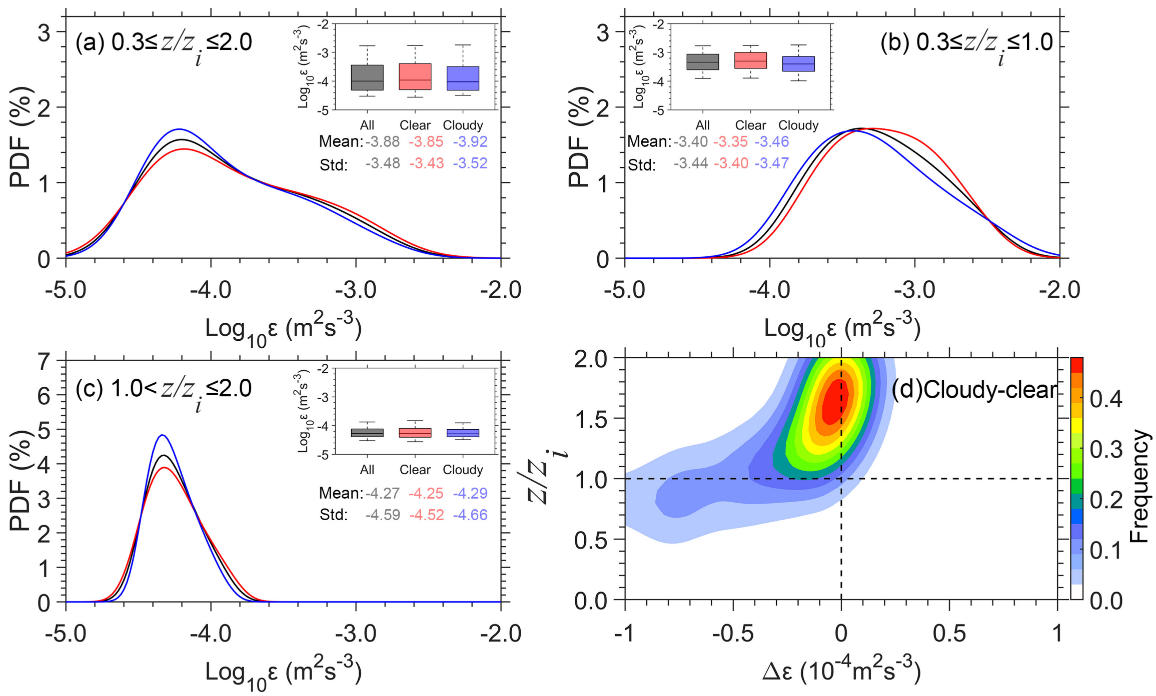

Figure 5. PDF of daytime $Log_{10}\varepsilon$ (a) in the whole lower troposphere (0.3≤z/z_i≤2.0), (b) in the PBL (0.3≤z/z_i≤1.0) and (c) above the PBL (1.0<z/z_i≤2.0) over the TP under all-sky (black), clear-sky (red) and cloudy-sky (blue) conditions, respectively. (d) Normalized contoured frequency by altitude diagram (NCFAD) for the difference of ε between cloudy-sky and clear-sky conditions (Δε) over the TP. Note that z_i denotes the depth of the PBL, the height (z) and turbulence dissipation rate (ε) is normalized by z_i in order to give a nondimensional vertical coordinate in the form of z/z_i.

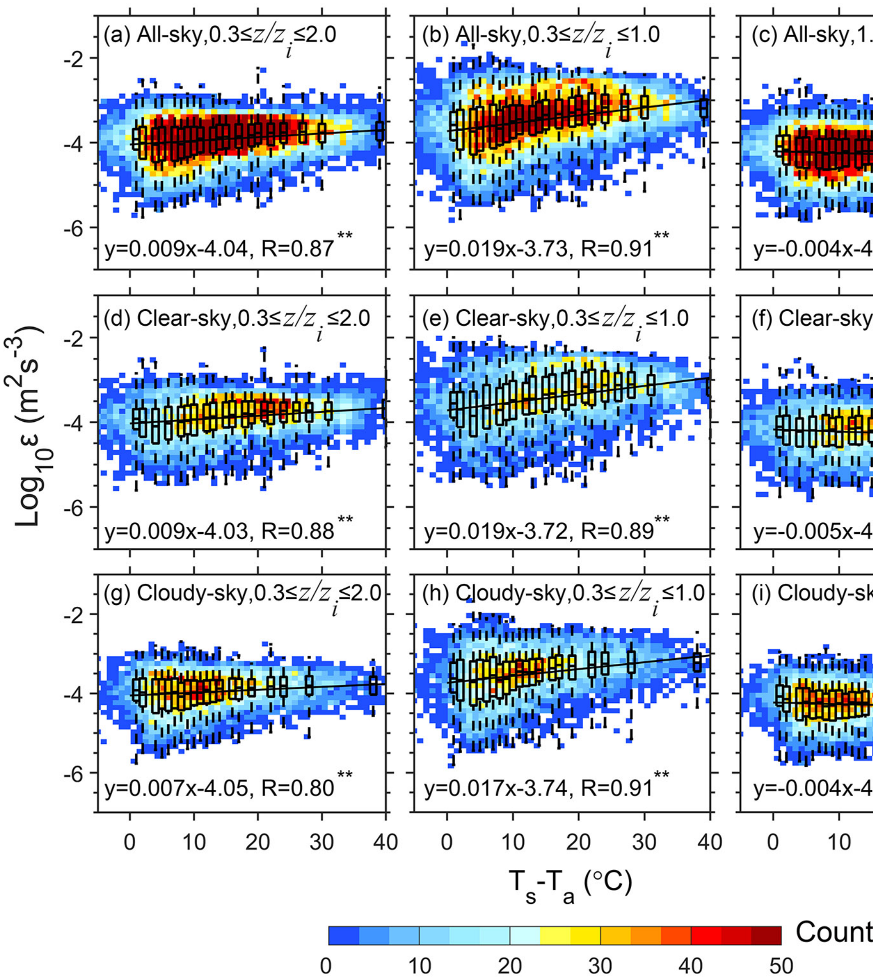

Figure 6. Scatter plots (blue dots) of $Log_{10}\varepsilon$ estimated from the measurements of RWPs in the whole lower troposphere (0.3≤z/z_i≤2.0, a, d, g), in the PBL (0.3≤z/z_i≤1.0, b, e, h) and above the PBL (1.0<z/z_i≤2.0, c, f, i) over the TP as a function of $T_s - T_a$ under all-sky (a-c), clear-sky (d-f) and cloudy-sky conditions (g-i), respectively. Also overlaid are their corresponding box and whisker plots and regression linear equations and correlation coefficients in each panel, where all $T_s - T_a$ samples are divided into twenty bins, each of which has the same sample size. Note that the median is shown as a line whereas the outer boundaries of the boxes represent 25 and 75 quartiles and the dashed lines present interquartile range (IQR). The superscripts * and ** for R indicate that the regression slopes are statistically significant at $p < 0.05$ and $p < 0.01$ levels, respectively.

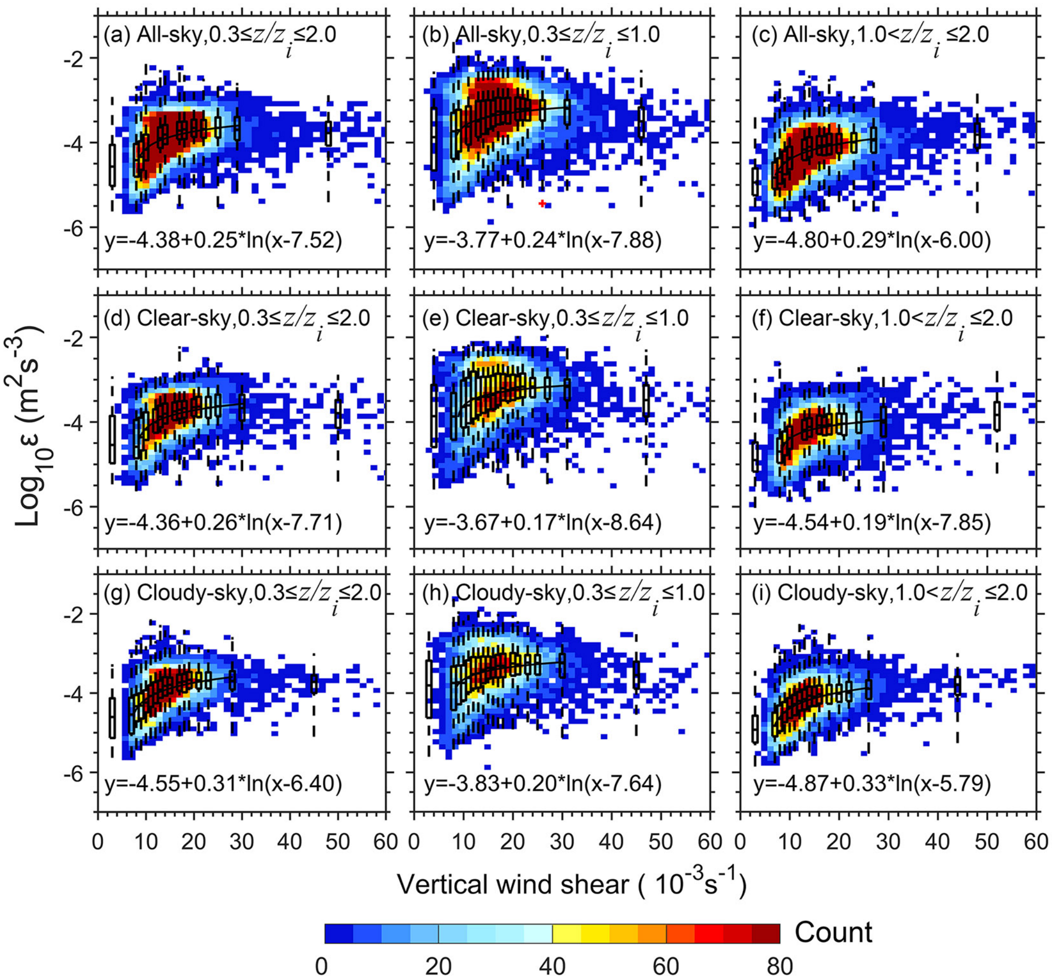

Figure 7. Scatter plots of $Log_{10}\varepsilon$ estimated from the measurements of RWPs in the whole lower troposphere (0.3≤z/z_i≤2.0, a, d, g), in the PBL (0.3≤z/z_i≤1.0, b, e, h) and above the PBL (1.0<z/z_i≤2.0, c, f, i) over the TP as a function of vertical wind shear (VWS) under all-sky (a-c), clear-sky (d-f) and cloudy-sky conditions (g-i), respectively. Also overlaid are their corresponding box and whisker plots and fitting equations in each panel, where all VWS samples are divided into twenty bins, each of which has the same sample size. Note that the median is shown as a line whereas the outer boundaries of the boxes represent 25 and 75 quartiles and the dashed lines present interquartile range (IQR).

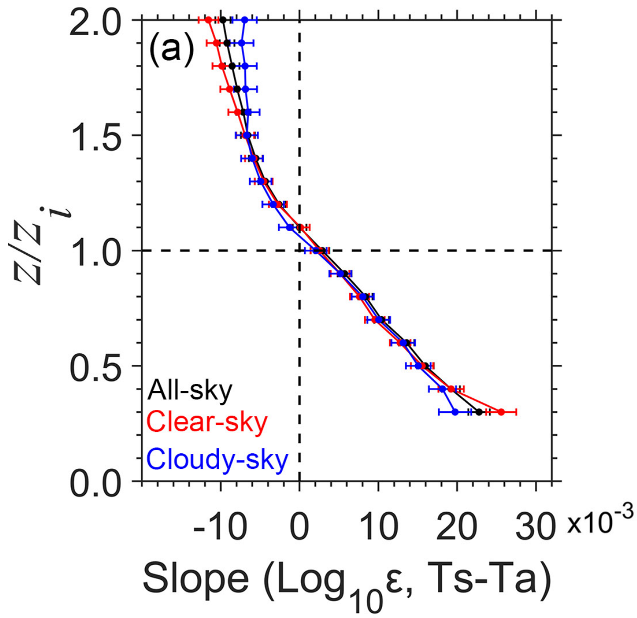

Figure 8. The vertical profiles of least squares regression slope between $Log_{10}\varepsilon$ and $T_s - T_a$ (a) and VWS (b) over the TP under all-sky (black), clear-sky (red) and cloudy-sky (blue) conditions, respectively.

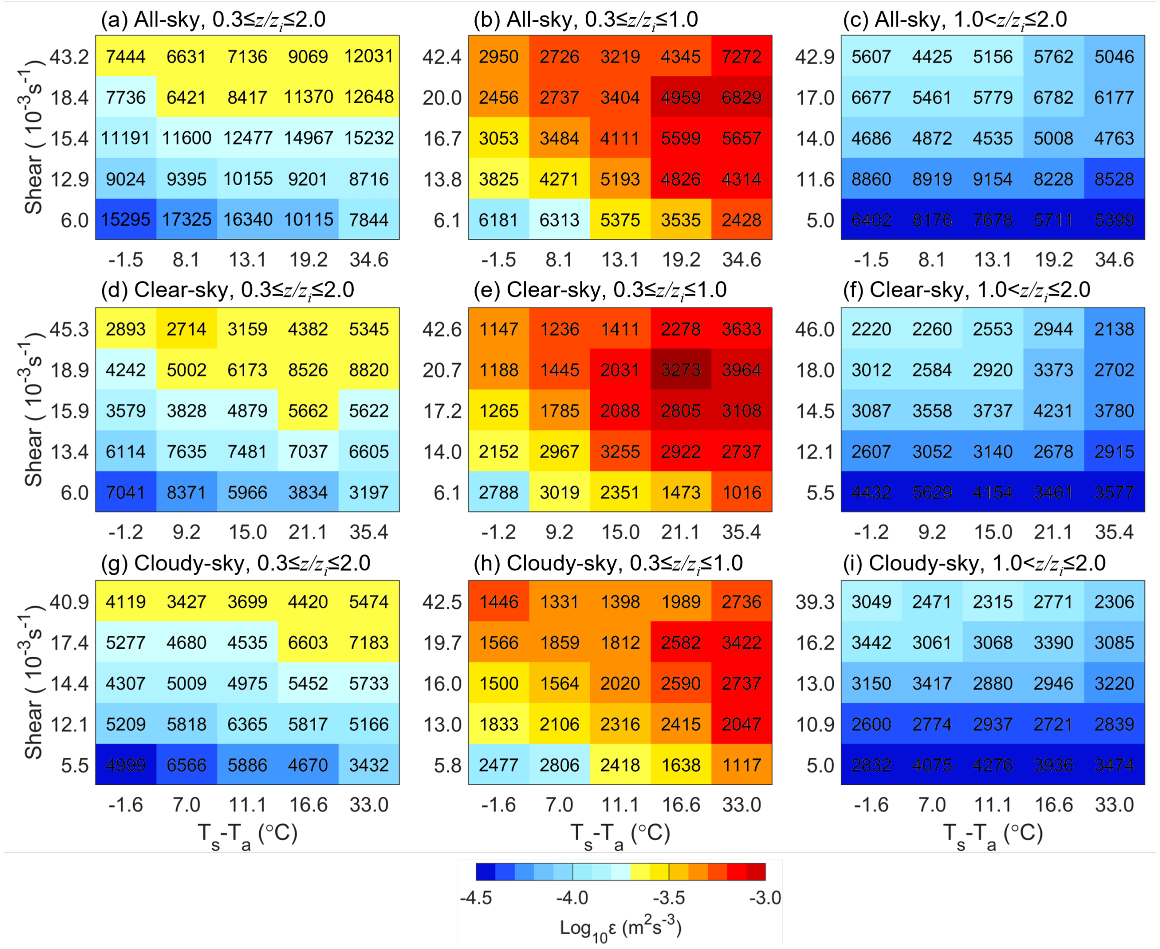

Figure 9. Joint dependence of $Log_{10}\varepsilon$ (color shading) on the VWS and $T_s - T_a$ within and above the PBL (a, d, g), in the PBL (b, e, h) and above the PBL (c, f, i) over the TP under all-sky (a-c), clear-sky (d-f) and cloudy-sky (g-i) conditions, respectively. The number given in each panel is the total number of samples used.

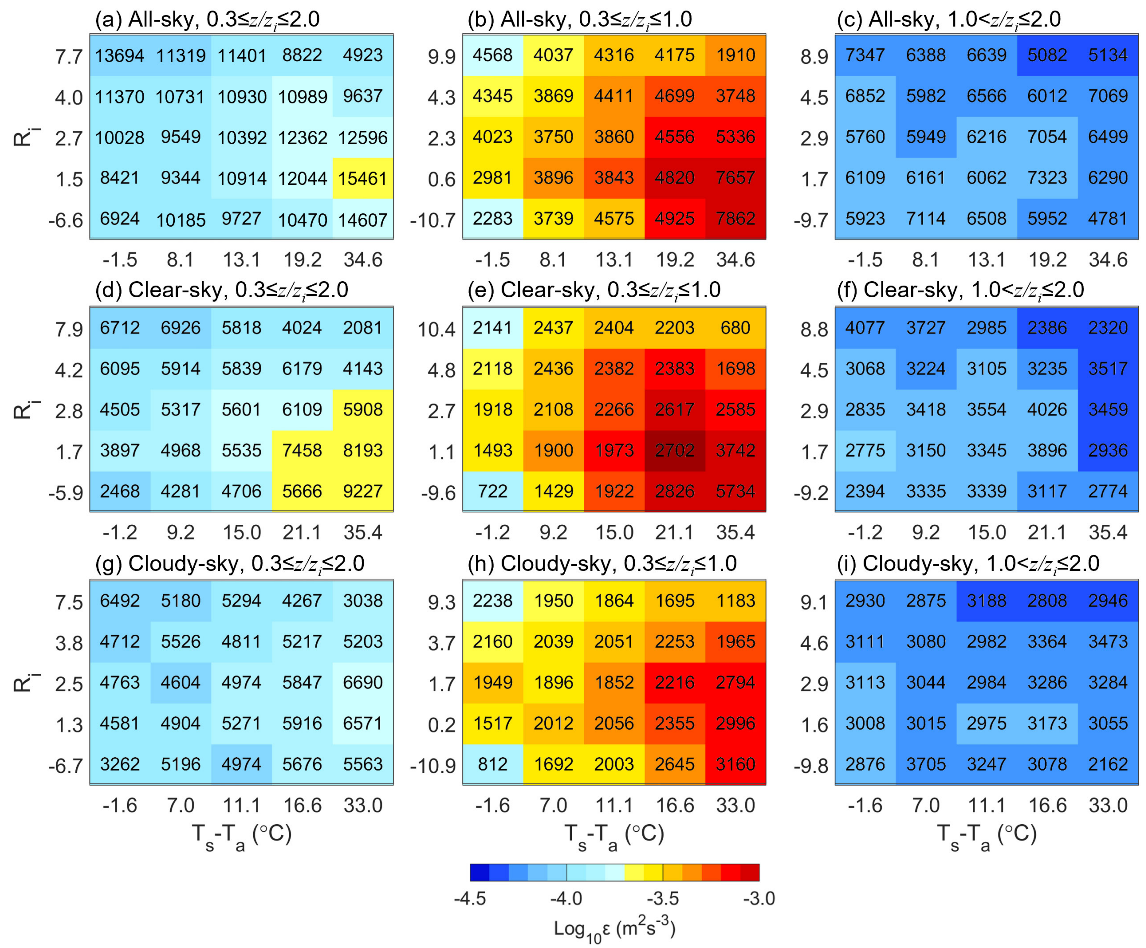

Figure 10. Joint dependence of $Log_{10}ε$ (color shading) on the gradient Richardson number (Ri) and $T_s - T_a$ in and above the PBL (a, d, g), in the PBL (b, e, h) and above the PBL (c, f, i) over the TP under all-sky (a-c), clear-sky (d-f) and cloudy-sky (g-i) conditions, respectively. The number given in each panel is the total number of samples used.